Experimental Mechanics (2023) 63:263–273
https://doi.org/10.1007/s11340-022-00914-x

RESEARCH PAPER

A Note On Measuring Mechanical Fields in 3-D Solids Using Digital Gradient Sensing and Refractive Index Matching

S. Dondeti[1] · C. Miao[1] · H. V. Tippur[1]

Received: 3 August 2022 / Accepted: 4 October 2022 / Published online: 18 October 2022

Abstract

Background The vision-based method of Digital Gradient Sensing (DGS) for performing full-field measurement of mechanical fields is currently limited to planar solids.

Objective In this work, a methodology to overcome this limitation in order to study 3-D phase objects (transparent solids) using transmission-mode DGS is described.

Methods The proposed approach employs the concept of refractive index matching of the solid body under investigation with its liquid surroundings. By placing the 3-D phase object of interest in a refractive index matching fluid environment of a flat-faced tank, refraction effects at the solid–fluid boundary can be eliminated.

Results This idea is demonstrated by visualizing and quantifying stress gradients in a PMMA cylinder subjected to a non-uniform stress field due to a concentrated force acting on one of its circular faces. The measurements are successfully compared with the analytical solutions based on Boussinesq equations.

Conclusions The proposed method enables investigation of mechanical fields in 3-D transparent solids by exploiting stress-optical effects in phase objects.

Keywords Full-field optical measurements · Stress analysis · 3-D phase solids · Refractive index matching · Vision-based methods

Introduction

Full-field, non-contact, quantitative visualization tools of experimental solid mechanics have become invaluable over the years for material modeling, mechanical characterization and discovery of new phenomena [1]. These include full-field coherent and incoherent optical techniques ranging from photoelasticity, interferometry to vision-based methods. Digital Gradient Sensing or DGS method was added to the tool kit in the last decade as a full-field, vision-based optical technique to quantitatively visualize mechanical fields in solids [2]. This method exploits elasto-optic effect exhibited by planar optically transparent (phase) solids to evaluate small angular deflections of light rays relative to a reference state due to non-uniform stress field. The angular deflections of light rays in two mutually perpendicular planes measured by this method allow quantification of stress gradient fields in the corresponding planes. By coupling the method with ultrahigh-speed photography, Periasamy and Tippur [3, 4] have extended DGS to study the evolution of stress gradients and quantify engineering parameters near stress concentrations during stress wave loading of PMMA plates. In a companion work, Periasamy and Tippur [5] have successfully extended it to quantify surface slopes and curvatures of specularly reflective opaque solids to demonstrate its feasibility to perform metrology of silicon wafers and reflective coatings. Subsequently, Jain and Tippur's work [6, 7] has extended the idea to study transient surface slopes/deformations of opaque solids with and without cracks subjected to in-plane and out-of-plane impact loading using high-speed photography. In recent years, DGS has been employed to study a range of challenging materials such as soft polymer gels [8] and stiff silicate glasses [9, 10]. It is particularly noteworthy that DGS has provided a means for mapping crack tip fields near dynamically growing cracks and revisit the long-standing problem of unprovoked crack branching in low toughness and high stiffness materials such

✉ H. V. Tippur
tippuhv@auburn.edu

[1] Department of Mechanical Engineering, Auburn University, Alabama, AL 36830, USA

as soda-lime glass. Dondeti and Tippur [11] have clearly demonstrated the superiority of DGS approach to others such as photoelasticity and digital image correlation for studying fracture mechanics of glasses.

The advent of DGS technique has led to its implementation as a full-field mechanical measurement tool in several other engineering mechanics problems. Hao et al. [12] have implemented DGS to study stress field interaction between a crack and an inclusion embedded in a polymer matrix. These authors have also utilized the method to measure mechanical fields associated with fiber pullout from a matrix [13]. In a separate work, Hao et al. [14] have successfully utilized DGS to visualize and quantify stresses that arise during curing of a polymer matrix. Zhang et al. [15] have extended DGS to the measurement of thermal stress fields at elevated temperatures that cause non-uniform refractive index changes in transparent materials. They have also examined the feasibility of DGS to evaluate thin film stresses and map topographic changes at elevated temperatures [16]. Zhang et al. [17] and Sundaram and Tippur [18] have studied mixed mode fracture mechanics of PMMA and polycarbonate sheet stock with the latter work focusing on the dynamic crack initiation and growth behaviors. Liu et al. [19] have employed DGS to study stress fields near blunt V-notches in elastic media. Interactions of a dynamically growing mode-I crack with a weak interface in elastically homogeneous PMMA bilayers have been investigated using DGS by Sundaram and Tippur [20, 21]. They have explored the conditions for a crack to grow across an interface with and without branching. A successful extension of the method to study strain rate effects in unidirectional CFRP coupons during mixed-mode crack initiation and growth has been reported by Miao and Tippur [22].

There have also been multiple reports on simplifying and enhancing capabilities of DGS methods. Miao et al. [23] have demonstrated the possibility of using measured stress gradient data from DGS along with a finite difference based least-squares integration to obtain stress fields and surface topographies of transparent and opaque solids, respectively. The feasibility of performing sub-micron scale measurements at microsecond intervals on large composite plates subjected to out-of-plane impact has been demonstrated by Miao and Tippur [24, 25]. These authors have also introduced two different optical arrangements capable of higher sensitivity angular deflection measurements using the principle of retro-reflection to double the optical path through the solid medium [26]. A simplified optical setup in reflection mode, without the use of a partial mirror, has been demonstrated by the same authors [27]. In a recent work, Fu et al. [28] have introduced a backlit speckle target to enhance the performance of DGS [28] methodology.

It should be noted that the above works employing DGS have all been carried out on planar (2-D) specimens. The present work is a step towards extending the technique to study non-planar 3-D solids. In the following, extending DGS to non-planar 3-D solids is introduced for the first time. The method is demonstrated on a PMMA circular cylinder subjected to an axially applied concentrated force. The measurements are compared with Boussinesq solutions for a point load acting on a half-space. The results along with potential measurement errors and future possibilities are then discussed and conclusions are drawn.

DGS for Transparent Planar Solids

The concept of transmission-mode DGS technique [2] under ambient conditions can be understood from the schematic in Fig. 1. The optical setup consists of a planar surface with sprayed, stamped, printed or natural random pattern/speckles (henceforth called the 'target'), a digital camera, illumination (incoherent broad-spectrum) lamps, and the transparent solid specimen. The random pattern on the target is first recorded by the camera in the reference or the undeformed state of the specimen. That is, the gray scale around a point P on the target plane (or x_o-y_o plane) is recorded by a pixel of the camera through point O on the specimen plane (x–y plane). Upon loading, the non-uniform stresses due to the imposed forces alter the local refractive index (n) of the specimen. Additionally, the Poisson effect (sometimes called the lens effect) causes non-uniform thickness (B) changes to occur locally as well.

A combination of the above two effects, commonly referred to as the elasto-optic effect, causes the light rays to deviate from the original path as they propagate through the stressed specimen. The random pattern on the target is once again recorded through the specimen in the deformed state or at the next load-step.

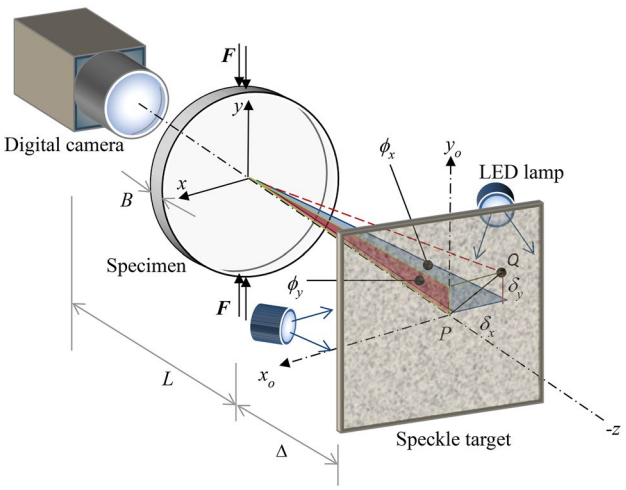

Fig. 1 The concept of transmission-mode Digital Gradient Sensing or DGS method to study transparent planar solids

Then, the gray scale of a neighboring point Q on the target plane is recorded by the same pixel of the camera through point O on the specimen plane after deformation. The local deviations of light rays between the two images can be quantified by correlating speckle images recorded in the deformed and reference states to determine *pseudo* speckle displacements δ_x and δ_y (Fig. 1). Knowing the distance Δ between the specimen plane and the target plane, these pseudo displacements (speckle shifts) can be converted into angular deflections of light rays ϕ_x and ϕ_y in the x–z and y–z planes with the z-axis coinciding with the optical/camera axis and x–y being the specimen plane. An opto-mechanical analysis based on the paraxial approximation has shown that the local angular deflections are related to the thickness-averaged gradients of in-plane Cauchy normal stresses as,

$$\left[\phi_{x;y} = \pm C_\sigma B \frac{\partial(\sigma_{xx} + \sigma_{yy})}{\partial(x;y)}\right] \tag{1}$$

where C_σ is the elasto-optic constant of the specimen material.

It should be noted that while recording the speckle field, the camera is focused on the target plane through the transparent specimen and not on the specimen. However, to elucidate the mechanical fields on the specimen plane, mapping $P(x_o, y_o)$ of the target plane to point $O(x, y)$ on the specimen plane is necessary. Using the pin-hole camera approximation, the coordinates of the target plane are related to the specimen plane coordinates as,$(x;y)(L + \Delta) = (x_o;y_o)L$.

DGS for 3-D Phase Solids

The concept behind extending DGS to non-planar 3-D phase objects requires elimination of refraction effects caused by the curvature of the solid being studied. The light rays traveling in a medium (say air) deviate from their initial path when they encounter a curved solid of a different refractive index due to the mismatch between the two media. In fact, this helps humans to visually perceive the shape of a transparent solid. However, refraction of light rays can be prevented by matching the refractive index of the 3-D solid with that of the surrounding medium. That is, submerging the solid body in a refractive index matching fluid medium with its index identical to that of the solid would eliminate bending of light rays at the solid–fluid interface. Upon mechanical loading of the solid, deformations are confined to the solid body allowing DGS method to proceed as intended in its traditional setup (Fig. 1). It is worth noting that this idea has been exploited in both solid [28–30] and fluid mechanics [31–33] communities previously. Some notable publications in the former category include scattered light photoelastic investigations on 3-D frozen-stress models immersed in index matching fluid in containers with flat windows/faces [28, 29]. Srinath et al. [30] have also used refractive index matching concept to quantitatively visualize maximum in-plane shear stress fields near cracks in cylindrical tubes subjected to torsion using 2-D photoelasticity. In the latter category, Budwig [31] has presented techniques for refractive index matching by choosing different solid and fluid materials and methods of tuning the match. The index matching approach is also popular in particle image velocimetry to achieve unobstructed optical paths for illumination and image acquisition. Bai and Katz [32] have presented data for sodium iodide solution of different concentrations to vary refractive index precisely in the range of 1.33 to 1.51 to match different phase objects. Vulprecht et al. [33] report the application of this idea to study flow in granular media.

The feasibility of the above idea is demonstrated in Fig. 2. A random speckle pattern on a target plane in air was recorded by a digital camera positioned normally to it and the resulting image of well-focused speckles is shown in Fig. 2(a). The same step was repeated next by placing a circular 50 mm diameter PMMA cylinder in front of the target plane without disturbing the camera settings or its location. In the latter case, the mid-plane of the solid cylinder was situated at a distance of ~ 75 mm beyond the cylinder in front of the target. The resulting image is shown in Fig. 2(b). It shows severe blurring of the target plane speckles, ranging from a complete loss of information along the two upright (vertical) edges to partial yet substantial loss speckle discernibility at the center of the intervening cylinder whereas regions outside the cylinder are still in sharp focus as to be expected.

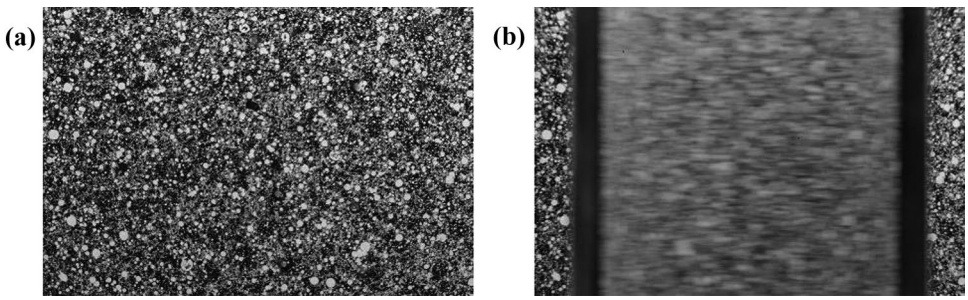

Fig. 2 Random speckles photographed off a target normally in air **a**, through a transparent upright PMMA cylinder (50 mm dia.) placed in front of the target **b**

In Fig. 3, the same speckle target was photographed through the upright PMMA cylinder with a similar optical setup used in Fig. 2 but this time while the cylinder was kept submerged in a flat-faced transparent PMMA tank filled with mineral oil; the top-view of the optical setup used is shown in Fig. 3(a). Since the refractive index of mineral oil matched with that of PMMA rather closely (refractive index values to follow in the next section), the speckles on the target plane are now clearly visible over the entire width of the 3-D solid, all the way to the edge of the cylinder (Fig. 3(b)). By matching the refractive indices to a higher degree, the residual blurriness of speckles along the highlighted edges of the cylinder could be eliminated altogether.

It should be emphasized here that the idea of using a flat-faced tank and refractive index matching fluid to surround the arbitrarily shaped solid volume reduces the problem to recording speckles though a rectangular volume of combined solid and fluid media of a single refractive index. It thus, essentially modifies the problem to traditional DGS approach used for planar solids.

Experiments

A schematic of the experiment setup used for the demonstration of mechanical field measurements using the refractive index matching approach is as shown in Fig. 4(a). It consists of an open-top, 152 mm × 108 mm × 120 mm flat-faced transparent tank made of PMMA (refractive index ~ 1.491) sheets shown in Fig. 4(b). A solid circular PMMA cylinder of 50 mm diameter and 75 mm height was positioned upright at the center of the rigid base/platform (made of 12.5 mm thick aluminum plate) of the tank. As shown in the inset of Fig. 4(b), the tank was filled with mineral oil (refractive index 1.475 under ambient conditions for a wave length of 550 nm) until the PMMA cylinder was fully submerged in oil with a ~ 30 mm fluid column over and above the top surface of the cylinder. The oil-filled tank with the PMMA cylinder was situated in the workspace of an Instron 4465 testing machine platform. A 12.5 mm spherical steel ball, wedged in a V-block fixture attached to the crosshead, was pressed into the top circular face of the upright cylinder to mimic a point load acting on a planar surface of a solid. The moving crosshead of the testing machine was fitted with a 5 kN Load cell to measure the applied force.

A speckle target with random, spray-painted, black/white speckles on a planar sheet was positioned behind the tank, parallel to its rear face and normal to the camera axis. The distance between the center of the cylinder on the mid-plane (x–y plane) of the cylinder and the target plane was 70 mm. A PointGrey digital camera with a 2048 × 2048 pixels sensor and 10-bit gray scale resolution was used to record the random speckles on the target plane at a rate of 5 frames per second. The camera fitted with a 18–208 mm macro zoom lens was positioned in front of the tank at a distance of approximately 1050 mm and focused on the target plane through the liquid-filled tank (magnification/scale factor = 45 μm/pixel). A pair of broad-spectrum lamps was used to uniformly illuminate the target plane. A laser-leveling device was used to ensure that the tank faces are normal to the camera.

Once the optical arrangement was complete, the crosshead of the loading machine along with the loading fixture was lowered into the tank until the steel ball made contact with the top of the cylinder. The disturbances in the fluid environment due to the crosshead motion was allowed to settle down and let any trapped air bubbles escape to the top of the fluid column and out of the field-of-view before conducting the experiment. The field-of-view included the region of the cylinder directly below the loading point on the top surface of the cylinder. The specimen was loaded monotonically from a no-load condition to a maximum load of 1000 N in displacement control mode at a crosshead speed of 0.005 mm/sec. The random speckle images were captured during the experiment in 100 N increments.

The recorded images at different load levels were paired with a reference image in the no-load condition and 2-D

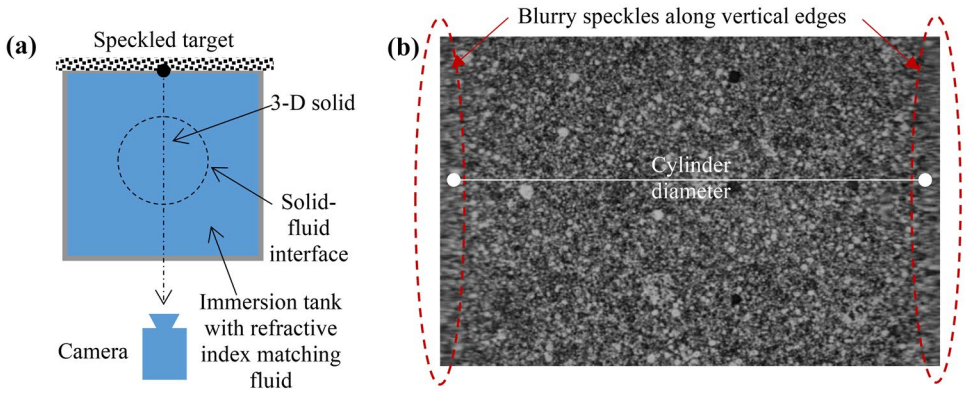

Fig. 3 Random speckles photographed through a 50 mm diameter PMMA cylinder immersed in mineral oil **b** using the optical setup (top-view) **a**

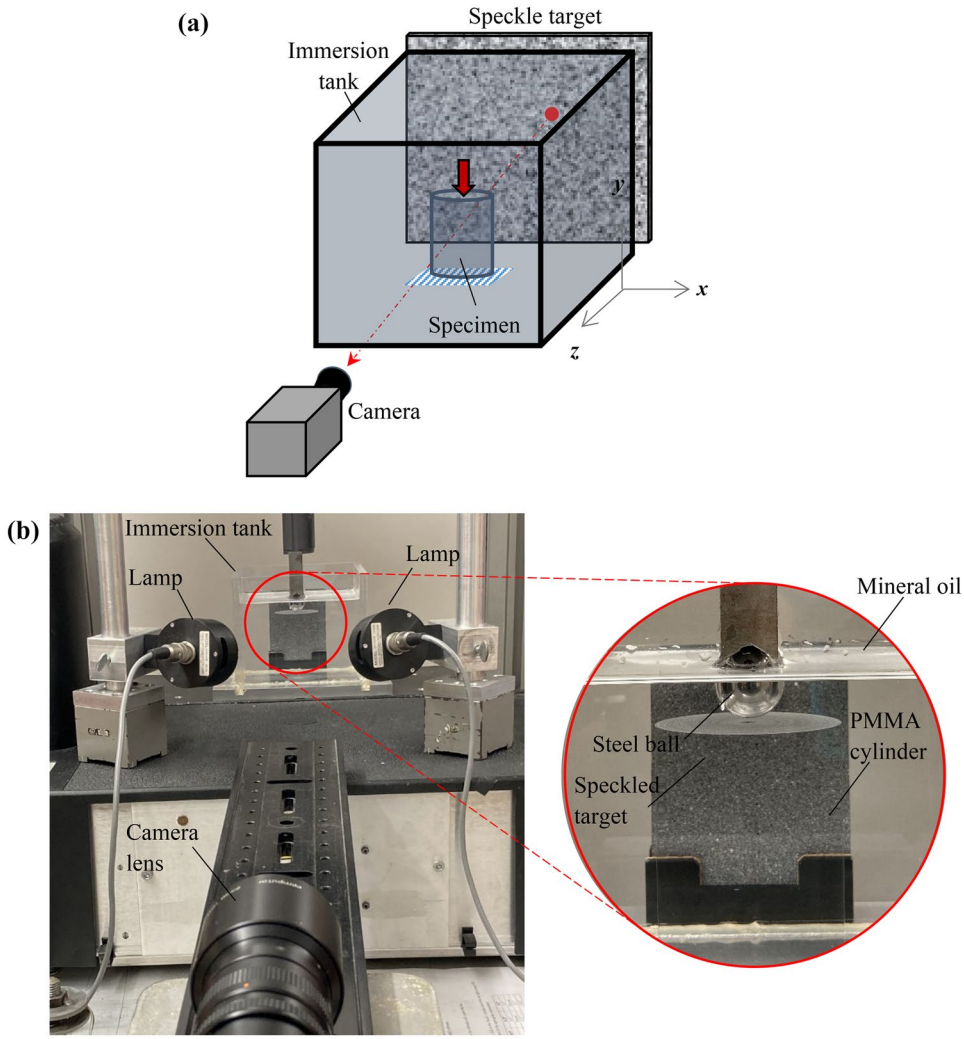

Fig. 4 Schematic of the optical setup **a** and experimental setup for DGS to study stress fields in 3-D objects **b**

digital image correlation using a commercial image analysis software – ARAMIS – was carried out. Each recorded image was segmented then into 30×30 pixels sub-images/facets and a sub-image step of 5 pixels (25 pixel overlap between sub-images) was used during image analysis. The correlation of images at each load level yielded 193×230 array of two orthogonal *pseudo* displacement components due to the stress-optic effect in the solid cylinder caused by the imposed stress field.

Working Principle

Under isothermal conditions, the optical path length S through the immersion tank is $S = nB_0$ where n and B_0 denote the nominal refractive index of the medium and the physical distance through the tank, respectively. Thus, the change in the optical path δS caused by the imposition of a mechanical field consists of a sum of changes in the refractive index, δn, and the physical distance, δB_0. When the refractive index of the solid and the liquid in the tank are matched, δB_0 term vanishes. Thus, the optical path difference δS at a generic point between the reference and deformed states of the specimen can be related to the refractive index changes δn as,

$$\delta S(x, y) = \int \delta n(x, y, z)\, dz \tag{2}$$

where δS is due to stress-induced refractive index variation integrated over the specimen thickness along the optical axis (z-axis) since only the solid suffers mechanical deformation in the fluid-filled tank. From the stress-optic principle [35], for an optically isotropic solid, $\delta n = D\left(\sigma_{xx} + \sigma_{yy} + \sigma_{zz}\right)$ where D is the stress-optic constant of the material and σ_{ij} are the Cauchy stress tensor components. Under paraxial conditions, the optical path changes are related to angular deflections of light rays as [2],

$$\phi_{x;y} = \frac{\partial(\delta S)}{\partial x;y} \tag{3}$$

where ϕ_x and ϕ_y are angular sweeps in the x–z and y–z planes with the z-axis coinciding with the camera axis and x–y plane is defined as the mid-plane of the specimen. Therefore, the angular deflections of light rays are proportional to spatial gradients of $(\sigma_{xx} + \sigma_{yy} + \sigma_{zz})$. It should be noted that unlike traditional DGS, here the measured angular deflections are unaffected by the Poisson effect that produces additional bending of light as it enters the solid. Thus, the measurements here are related to mechanical stresses as,

$$\phi_{x;y} = D\frac{\partial \hat{I}_1}{\partial x;y} \tag{4}$$

where $\hat{I}_1\left(= \int_{z_1}^{z_2} (\sigma_{xx} + \sigma_{yy} + \sigma_{zz})dz\right)$ is the integrated value of the first invariant of the Cauchy's stress tensor (hydrostatic stress) and the limits of integration correspond to the 'thickness' of the solid body along the line-of-sight. The stress-optic constant D needs to be known a priori to quantify the mechanical fields from measured angular deflections of light rays. For many common material systems such as PMMA, glass, epoxy, to name a few, the value of D can be readily found in the literature [34, 35]. When not available, a calibration experiment would necessary to evaluate this material constant. A calibration procedure such as the one outlined in Ref. [18] can be used to find C_σ when necessary.

For the purpose of the present work, the elasto-optical constant C_σ that accounts for combined stress-optic and Poisson effects in equation (1) is expressed as,

$$C_\sigma = D - \frac{\nu}{E}(n - n_{air}), \tag{5}$$

with refractive index of air, n_{air}, assumed to be equal to 1. For PMMA specimen used in this work C_σ is -0.9×10^{-10} m^2/N under quasi-static conditions [2]. Knowing the values of elastic modulus (=3.3 GPa [3]) and Poisson's ratio (=0.35) and refractive index (n=1.491 at a wave length of 550 nm) for PMMA, the stress optic constant can be found and is -0.35×10^{-10} m^2/N.

Boussinesq Equations

Consider the classical Boussinesq's problem of a concentrated force P acting normal to a semi-infinite homogeneous isotropic elastic solid (Fig. 5). Due to the axisymmetric nature of the problem, normal stresses in cylindrical coordinates can be expressed as [36],

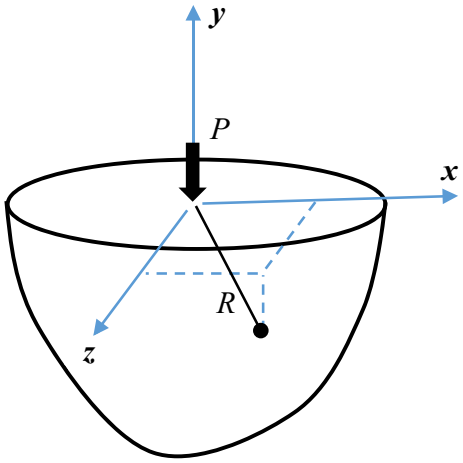

Fig. 5 Concentrated force normal to a semi-infinite homogeneous isotropic elastic solid

$$\begin{aligned} \sigma_{rr} &= \frac{P}{2\pi R^2}\left[\frac{3(x^2+z^2)y}{R^3} + \frac{(1-2\nu)R}{(R-y)}\right] \\ \sigma_{\theta\theta} &= -\frac{(1-2\nu)P}{2\pi R^2}\left[\frac{y}{R} + \frac{R}{(R-y)}\right] \\ \sigma_{yy} &= \frac{3Py^3}{2\pi R^5} \end{aligned}, \tag{6}$$

where $r = \sqrt{x^2+z^2}$ and $R = \sqrt{r^2+y^2} = \sqrt{x^2+y^2+z^2}$. Hence, the first invariant of stress I_1 is,

$$I_1 = \frac{(1+\nu)Py}{\pi R^3}. \tag{7}$$

From equations (2)-(7), the expression for the optical path difference δS in terms of mechanical stresses is,

$$\delta S = D\hat{I}_1 = \frac{P(1+\nu)D}{\pi}\int_{z_1}^{z_2} \frac{y}{\left(x^2+y^2+z^2\right)^{3/2}}\,dz. \tag{8}$$

The limits of the above integral for a circular cylinder of radius B are $-z_1 = z_2 = \sqrt{B^2-x^2}$. Thus, the optical path difference δS becomes,

$$\delta S = \frac{P(1+\nu)D}{\pi}\left(\frac{\sqrt{B^2-x^2}}{\sqrt{B^2+y^2}}\right)\left(\frac{2y}{x^2+y^2}\right). \tag{9}$$

This leads to angular deflection of light rays related to the mechanical fields as,

$$\begin{aligned} \phi_x &= \frac{\partial(\delta S)}{\partial x} = \frac{P(1+\nu)D}{\pi}\left(\frac{2y\left(x^3-2B^2x-xy^2\right)}{\sqrt{B^2+y^2}\left(x^2+y^2\right)^2\sqrt{B^2-x^2}}\right) \\ \phi_y &= \frac{\partial(\delta S)}{\partial y} = \frac{2P(1+\nu)D}{\pi}\left(\frac{\left(-2y^4-B^2y^2+B^2x^2\right)\sqrt{B^2-x^2}}{\left(B^2+y^2\right)\left(x^2+y^2\right)^2\sqrt{B^2+y^2}}\right) \end{aligned}. \tag{10}$$

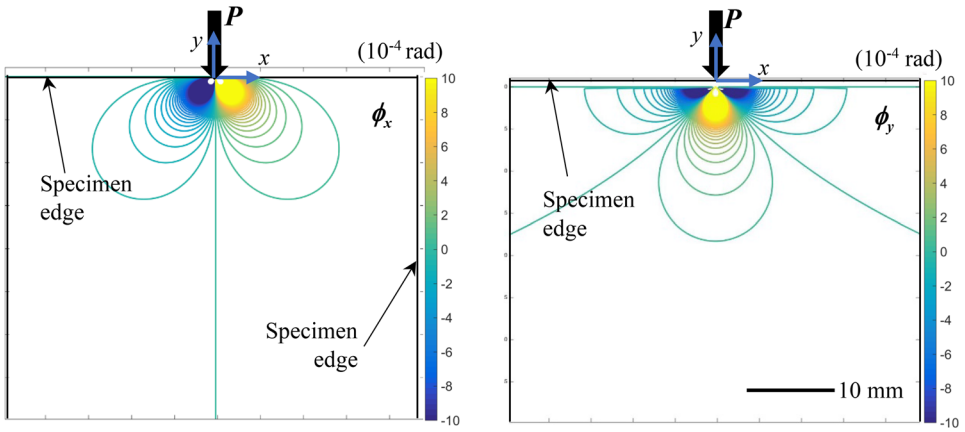

Fig. 6 Analytical angular deflection ϕ_x and ϕ_y (equation (9)) contours near loading point ($P=500$ N, $D=-0.35\times10^{-10}$ m^2/N, $\nu=0.35$, $B=25$ mm).

Results

The contours of constant angular deflections of light rays in two mutually orthogonal planes obtained from equation (10) are plotted in Fig. 6. As to be expected, the concentrated force produces a stress singularity at the point of application and the resulting stress gradient contours clearly reflect that. Furthermore, the ϕ_x and ϕ_y contours are antisymmetric and symmetric, respectively,

Figure 7 shows contour plots of measured angular deflection of light rays ϕ_x and ϕ_y from the experiment along with a pair of speckle images in the reference and deformed (load = 500 N) states of the PMMA cylinder. The qualitative similarities between the measurements and the predictions (Fig. 6) are self-evident. As in the theoretical counterparts, the ϕ_x and ϕ_y contours are antisymmetric and symmetric, respectively, relative to the loading axis. The data close to the loading point is smeared due to the finite scale factor that has resulted in some loss information while correlating speckles in regions of severe deformations. This is also partly attributed to the finite size of sub-images used for correlating the images in the reference and deformed states, a general drawback of vision-based methods due to spatial/pixel resolution of digital cameras. Other differences

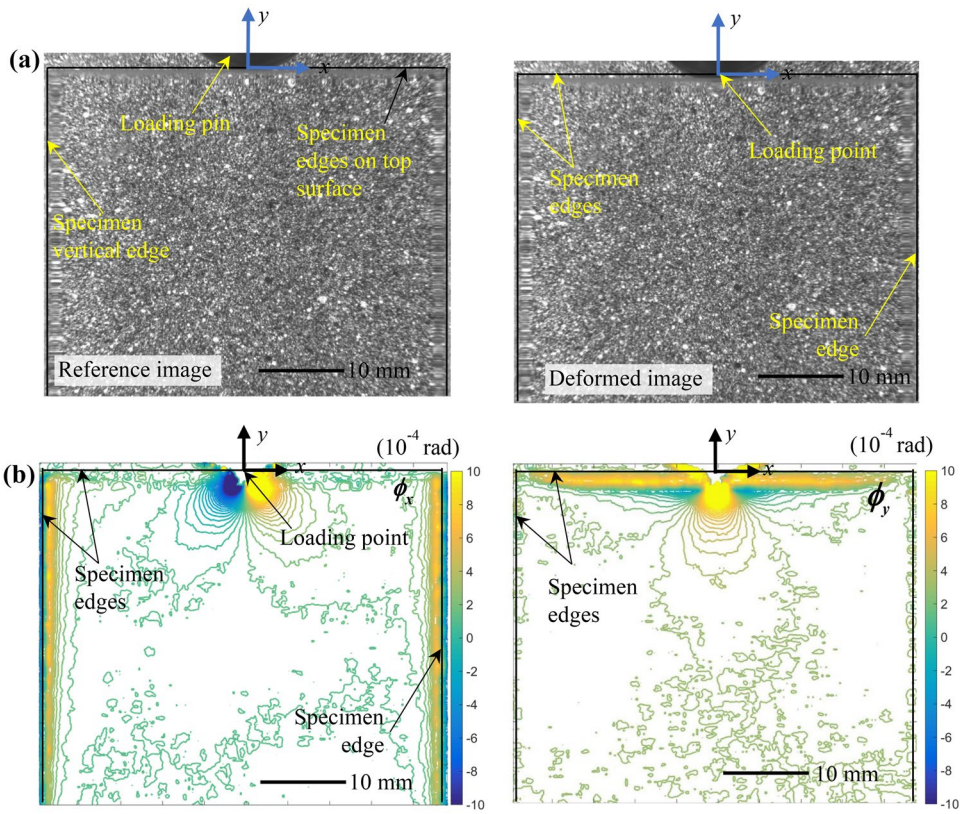

Fig. 7 Optical measurements. **a** Recorded speckle images in the undeformed and deformed ($P=500$ N) states. Angular deflections of light rays ϕ_x and ϕ_y contours near the loading point

between theoretical and experimental results include the finite dimensions of the cylinder unlike the theoretical solution based on a solid semi-infinite half-space.

Next, to assess the optical measurements quantitatively, the measured angular deflections of light rays caused by the imposed load along dominant directions $\theta = 0^o$ and $\theta = \pm 45^o$(with respect loading direction) in x–z and y–z planes, respectively, are compared with the Boussinesq's solutions (equation (10)). In Fig. 8(a) and (b), ϕ_x and ϕ_y values are plotted relative to the normalized radial extent $r/2B = 0.25$ where $2B$ is the diameter of the cylinder and r is the radial distance from the origin. The standard error bars in these two plots are due to uncertainty of identifying the origin. That is, locating the origin has an uncertainty of one-step size or 5 pixels in the x- and y-directions relative to the nominal. The overall data trends match the theoretical predictions quantitatively even at relatively small distances of ~ 2 mm from the loading point at the chosen optical magnification.

In Fig. 8(a), mismatch in the ϕ_x data in $\pm 45^o$ of loading direction is somewhat evident in the experimental data due to plausible errors in anchoring the origin in the images. Otherwise, an excellent agreement is achieved over the entire measurement window when the two data sets are averaged. The ϕ_y data agrees well with the theory close to the loading point, say up to $r/2B = 0.15$. Beyond that, a small yet noticeable offset (see inset) persists between measurements and the theory. This can be attributed to the finite height of the cylinder used during experiments which in turn produces a non-zero state of stress in the PMMA cylinder away from the loading point. This is unlike the theoretical solution where the state of stress decays to a zero state of stress far away from the loading point.

The potential error due to optical misalignment of the immersion tank relative to the camera was also tested. The experiments were repeated with approx. $\pm 1°$ misalignment relative to the optical axis. Measurements from two such attempts besides the one in Fig. 8(a) are presented in Fig. 8(c). The agreement between the three sets of data is evidently robust.

The full-field optical data can also be valuable for extracting engineering parameters of interest in 3-D problems. In the current exercise, the imposed load on the cylinder at various instants of time (or crosshead displacement) could be treated as an engineering parameter of interest. Accordingly, the measured optical data for both ϕ_x and ϕ_y fields at various time instants or load-steps during experiments were used in conjunction with equation (10) and over-deterministic least-squares analysis to compute the concentrated force that produced the corresponding refractive index change. A plot of thus measured force from each angular deflection field is compared to the one recorded by the load-cell of the testing machine in Fig. 9. The solid symbols represent the measured force from the two separate fields and the solid line represents the load-cell data. The agreement between all three is very good until the largest imposed force of 1000 N on the cylinder during this experiment. The maximum deviation between the measurements and the load-cell is less than 10% with most data in the better than 5% deviation range. Furthermore, the nonlinearity in the load–deflection plot shows a Hertzian contact response between the spherical ball and planar PMMA face, as expected.

Discussion

The full-field optical measurements presented above for a 3-D solid object made of PMMA demonstrates the feasibility of DGS to perform mechanical field quantification in simply connected phase objects of known dimensions. By adopting the refractive index matching concept, the requirement that the solid body under investigation be a planar object has been removed. It should be noted that in doing so the sensitivity of the tradition DGS method based on the elasto-optic effect is somewhat reduced because the refractive index matching eliminates the role Poisson effect plays on the overall deflection of light rays besides the stress-optic effect due to refractive index changes. That is, the cumulative effect of stress-optic and Poisson effects in traditional DGS is reduced to just the former. However, this issue may not be significant in general since the measurement sensitivity of DGS can be offset by increasing the distance between the target and the specimen.

Another notable aspect is regarding the degree of refractive index match between the solid and liquid environments to perform measurements. DGS being a comparative method that quantifies *pseudo* speckle shifts between reference and deformed states of the object, well-defined speckle recordings without smearing of the gray scale is essential to achieve successful image correlation in order to quantify speckle shifts due to refractive index change. To assess this, equation (5) can be rewritten as,

$$D_s = \left(C_\sigma\right)_s + \left(\frac{\nu}{E}\right)_s (n_s - n_f), \tag{11}$$

where subscript s and f are used to denote the solid body and fluid medium surrounding it. When the refractive indices of the two phases are perfectly matched, or $(n_s - n_f) = 0$, the second term on the RHS of equation (11) vanishes and the stress-optical constant becomes equal to the elasto-optical constant of the solid specimen. On the other hand, when the refractive index match is imprecise, D_s can be viewed as $D_s + \delta D$ where δD is the error in the stress-optical constant due to the *residual* Poisson effect that is not eliminated. The value of δD can be estimated for the present exercise as $(n_s - n_f) \approx 0.016$ since nominal values for both n_s and n_f are

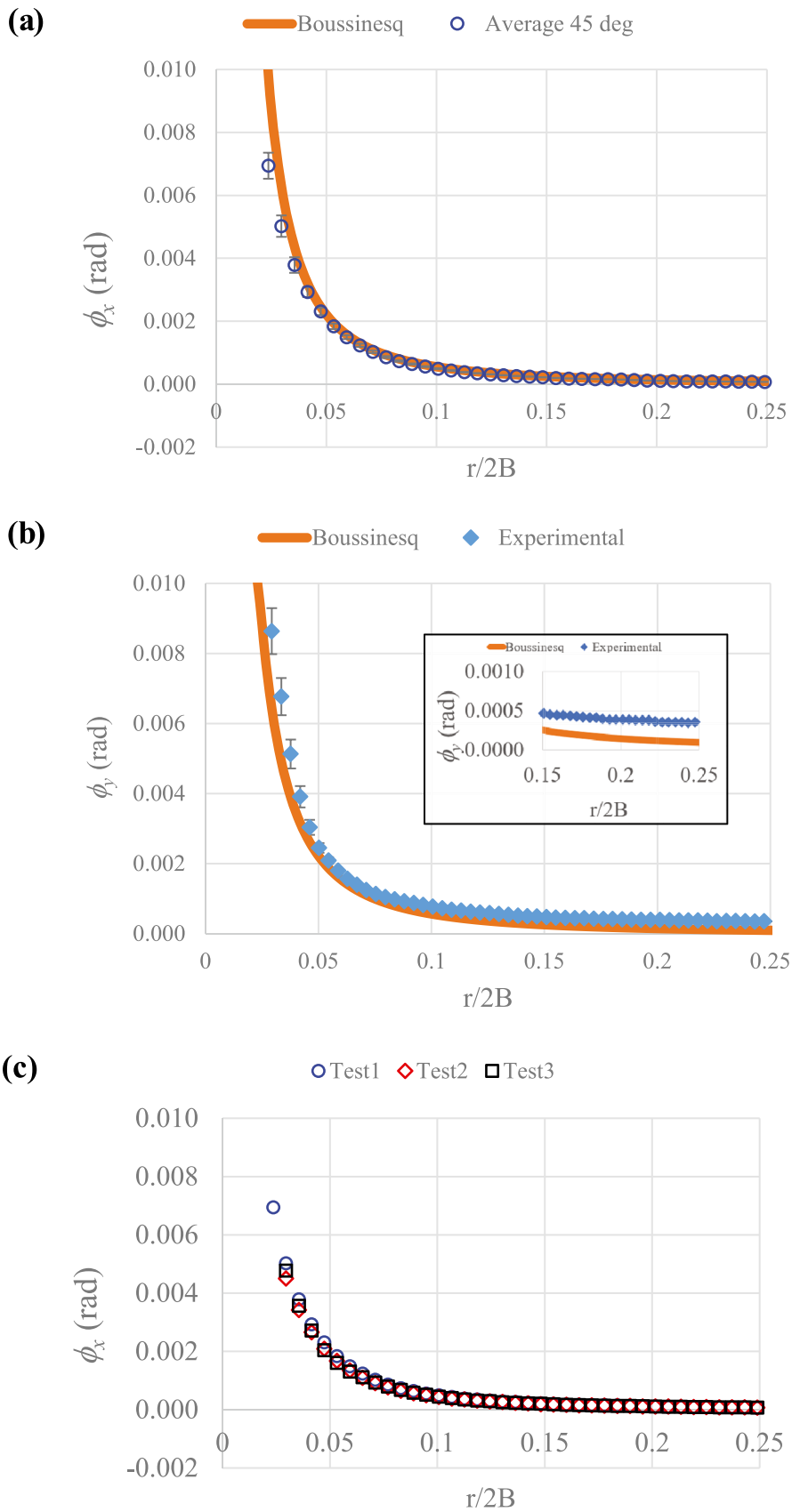

Fig. 8 Comparison of analytical and experimental angular deflections *averaged* $|\phi_x|$ in $\pm 45°$ to loading direction **a**, ϕ_y in loading direction **b** and averaged $|\phi_x|$ in $\pm 45°$ to loading direction from three tests (**c**) at $P = 500$ N applied load

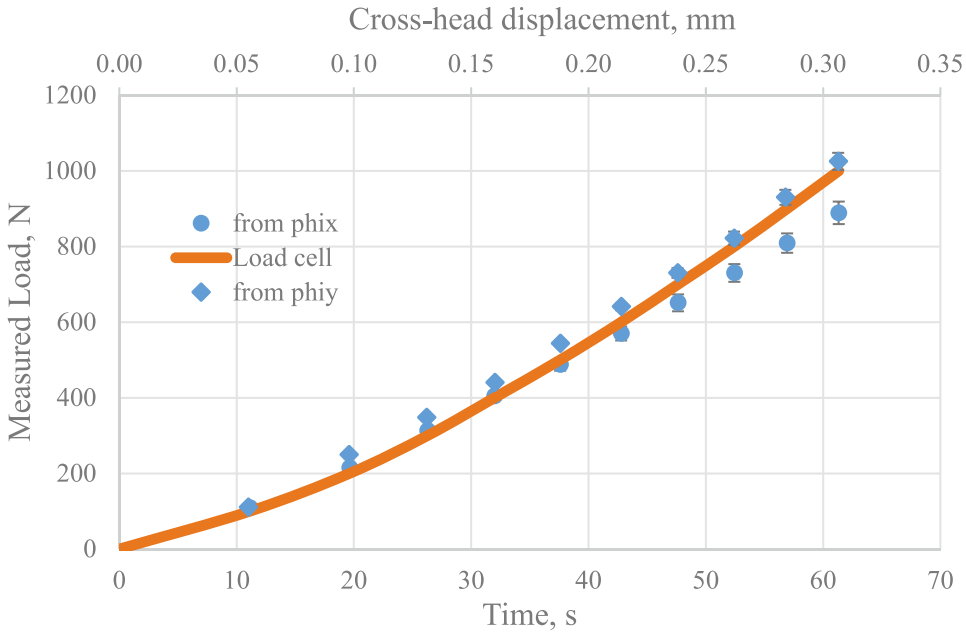

Fig. 9 Load histories comparison from measured angular deflections ϕ_x and ϕ_y with the applied loads

known. That is, the second term on the right-hand side of the equation has a numerical value of 1.7×10^{-12} m^2/N relative to D_s (=D in Equation 4) of -0.35×10^{-10} m^2/N. Since ϕ_x and ϕ_y in equation (10) are directly proportional to D, the errors in the angular deflections due to refractive index mismatch effect can be readily computed due to this imperfect refractive index match and is approx. 5%.

Lastly, it is worth noting that, if necessary, the two orthogonal stress gradients of the cylinder can be integrated using a robust numerical scheme such as the one reported in Ref. [23] to obtain the first invariant of Cauchy stresses in the whole field when the boundary conditions are known. The method also has the potential to explore multiple interior planes of the solid body sequentially or simultaneously and evaluate the stress fields volumetrically [37]. That said, there are obvious limitations to the approach namely, (a) transparency requirement of the solid and the liquid media relative to the wavelength of light used in the investigation and, (b) requirement of a non-reactive fluid whose refractive index matches that of the solid. Furthermore, the ability of the method to explore other complex 3-D shapes including multiply-connected ones may be challenging and needs further investigation.

Conclusions

In this work, the feasibility of full-field Digital Gradient Sensing (DGS) method to study 3-D phase/transparent solid objects is demonstrated and is rather promising. The ability of transmission DGS to quantitatively visualize two orthogonal stress gradient fields in a PMMA circular cylinder subjected to a point force acting on one of its faces is shown. The elimination of refraction effects by submerging the solid body of interest in a flat-faced transparent tank filled with refractive index matching fluid is shown to enable imaging of random speckle decoration on the target plane through the PMMA cylinder without defocus or smear. This in turn facilitates successful correlation of the recorded speckle fields in the reference and deformed states of the solid to quantify pseudo speckle shifts in the whole field, allowing measurement of angular deflections of light rays due to refractive index changes in the solid due to mechanical stress. These angular deflections of light rays caused by the stress-optic effect can then be related to thickness-averaged stress gradients. The measured mechanical fields are directly compared to Boussinesq's analytical solution for an isotropic elastic solid and a good agreement between the two is observed.

Declarations

Ethical Approval This article does not contain any studies with human participants or animals performed by any of the authors.

Conflicts of Interest The authors declare that they have no potential conflicts of interest. HVT currently serves on the international advisory board of the journal.

References

1. Sharpe WN Ed (2008) Handbook of experimental mechanics. Springer

2. Periasamy C, Tippur HV (2012) A Full-Field Digital Gradient Sensing Method for Evaluating Stress Gradients in Transparent Solids. Appl Opt 51(12):2088–2097
3. Periasamy C, Tippur HV (2013) Measurement of Orthogonal Stress Gradients Due to Impact Load on a Transparent Sheet using Digital Gradient Sensing Method. Exp Mech 53:97–111
4. Periasamy C, Tippur HV (2013) Measurement of Crack-tip and Punch-tip Transient Deformations and Stress Intensity Factors using Digital Gradient Sensing Technique. Eng Fract Mech 98:185–199
5. Periasamy C, Tippur HV (2013) A Full-Field Reflection-Mode Digital Gradient Sensing Method for Measuring Orthogonal Slopes and Curvatures of Thin Structures. MEAS SCI TECHNOL 24(Paper # 025202):9
6. Jain AS, Tippur HV (2015) Mapping Static and Dynamic Crack-Tip Deformations using Reflection-Mode Digital Gradient Sensing: Applications to Mode-I and Mixed-Mode Fracture. J Dynamic Behav Mater 1:315–329
7. Jain AS, Tippur HV (2016) Extension of reflection-mode Digital Gradient Sensing method for visualizing and quantifying impact induced transient deformations and damage in solids. Opt Lasers Eng 77:162–174
8. Pasumarthy RKA, Tippur HV (2016) Mechanical and optical characterization of a tissue surrogate polymer gel. Polym Test 55:219–229
9. Sundaram BM, Tippur HV (2018) Full-field measurement of contact-point and crack-tip deformations in soda-lime glass. Part-I: Quasi-static loading. Int J Appl Glass Sci 9:114–122
10. Sundaram BM, Tippur HV (2018) Full-field measurement of contact-point and crack-tip deformations in soda-lime glass. Part-II: Stress wave loading. Int J Appl Glass Sci 9:123–136
11. Dondeti S, Tippur HV (2020) A comparative study of dynamic fracture of soda-lime glass using photoelasticity, digital image correlation and digital gradient sensing techniques. Exp Mech 60:217–233
12. Hao WF, Tang C, Ma YJ (2016) Study on crack-inclusion interaction using digital gradient sensing method. Mech Adv Maters Struct 23:845–852
13. Hao WF, Tang C, Yuan Y, Yao X, Ma YJ (2015) Experimental study on fiber pull-out in composites using digital gradient sensing technique. Polym Test 41:239–244
14. Hao WF, Chen X, Ma YJ (2016) Experimental Investigation on Curing Stress in Polymer Composite Using Digital Gradient Sensing Technique. Int Polym Proc 31:57–67
15. Zhang C, Qu Z, Hwang KC (2016) Digital Gradient Sensing Method to Evaluate Thermal Stress at Elevated Temperatures. Exp Mech 56:1123–1132
16. Zhang C, Qu Z, Hwang KC (2015) Full-field measurement of surface topographies and thin film stresses at elevated temperatures by digital gradient sensing method. Appl Opt 54(4):721–727
17. Zhang R, Guo R, Wang S (2014) Mixed mode fracture study of PMMA using digital gradient sensing method. 119:164–172
18. Sundaram BM, Tippur HV (2017) Dynamic mixed-mode fracture behavior of PMMA and polycarbonate using Digital Gradient Sensing. Eng Fract Mech 176:186–212
19. Liu W, Li LK, Qiao YX (2021) Local stress analysis of blunt V-notches using the digital gradient sensing method. Appl Opts 60:1489–1499
20. Sundaram BM, Tippur HV (2016) Dynamic Crack Growth Normal to an Interface in Bi-Layered Materials: An Experimental Study using Digital Gradient Sensing Technique. Exp Mech 56:37–57
21. Sundaram BM, Tippur HV (2016) Dynamics of crack penetration vs. branching at a weak interface: An experimental study. J Mech Phys Solids 96:312–332
22. Miao C, Tippur HV (2019) Fracture behavior of carbon fiber reinforced polymer composites: An optical study of loading rate effects. Eng Fract Mech 207:203–221
23. Miao C, Sundaram BM, Huang L, Tippur HV (2016) Surface profile and stress field evaluation using Digital Gradient Sensor,. Measurement Sci Technol 27(paper #095203)
24. Miao C, Tippur HV (2019) Reflection-mode digital gradient sensing method: Measurement accuracy. Opt Eng 58:044101
25. Miao C, Tippur HV (2018) Measurement of Sub-micron Deformations and Stresses at Microsecond Intervals in Laterally Impacted Composite Plates Using Digital Gradient Sensing. J Dynamic Behav Maters 4:336–358
26. Fu B, Li C, Dong B, Ou P (2020) Enhanced Digital Gradient Sensing Using Backlight Digital Speckle Target. Sensors 20:6557
27. Miao C, Tippur HV (2020) A simplified reflection-mode digital gradient sensing technique for measuring surface slopes, curvatures and topography. Opt Lasers Eng 124:105843
28. Ascough J (1981) A Review of the Scattered-Light Method in Photoelasticity. Opt Lasers Eng 2:215–228
29. Srinath LS (1969) Analysis of scattered-light methods in photoelasticity. Exp Mech 9:463–468
30. Srinath LS, Murthy NS, Hareesh TV (1983) Determination of Stress Intensity Factors for Cracks in Tubes under Torsion. Exp Mech 23:262-267
31. Budwig R (1994) Refractive index matching method for liquid flow investigations. Exp Fluids 17:350–355
32. Bai K, Katz J (2014) On the refractive index of sodium iodide solutions for index matching in PIV. Exp Fluids 55:1704
33. Vulprecht L, Gerstenberg C, Rauh C (2020) Refractive index matching of liquid and semi-solid materials to acrylic glass for optically measuring the mechanics of soft granular matter. Granual Mat (Article #47):22
34. Tippur HV, Krishnaswamy S, Rosakis AJ (1991) Optical Mapping of Crack Tip Deformations using the Methods of Transmission and Reflection Coherent Gradient Sensing: A Study of Crack Tip K-dominance. Int J Fract 52:91–117
35. Shukla A, Dally JW (2014) College House Enterprises, LLC. Experimental Solid Mech
36. Saad M (2009) Elasticity. Academic Press
37. Tippur HV (2021) A vision-based technique for measuring transient stress gradients in a 3-D phase objects. Provisional Patent Application 63/191,624. Auburn University, AL